



The predictive value of ^{18}F -FDG PET/CT radiomics for pleural invasion in non-small cell lung cancer



Annan Zhang^{a,1}, Meixin Zhao^{a,1}, Xiangxing Kong^b, Weifang Zhang^a, Xiaoyan Hou^a, Zhi Yang^b, Xiangxi Meng^{b,*}, Nan Li^{b,*}

^a Department of Nuclear Medicine, Peking University Third Hospital, 49 North Garden Road, Haidian District, Beijing 100191 Beijing, China

^b Key Laboratory of Carcinogenesis and Translational Research (Ministry of Education/Beijing), Department of Nuclear Medicine, Peking University Cancer Hospital & Institute, 52 Fucheng Road, Haidian, Beijing 100142, China

ARTICLE INFO

Keywords:

Non-small cell lung cancer
Pleural invasion
PET/CT
Radiomics

ABSTRACT

Objective: This study aims to develop and validate a PET/CT radiomics fusion model for preoperative predicting pleural invasion (PI) in non-small cell lung cancer (NSCLC) patients.

Methods: Data from Center A were divided into a training set ($n = 260$) and an internal validation set ($n = 111$), while data from Center B ($n = 99$) served as the external validation set. Radiomic features were extracted using PyRadiomics. Six feature screening methods and 12 machine learning methods were used to build clinical, PET/CT imaging, and radiomics fusion models. The best-performing model was selected based on accuracy, sensitivity, specificity, and area under the curve (AUC). A nomogram was created using logistic regression with clinical, PET/CT features, and Rad_score.

Results: The PET/CT radiomics fusion model exhibited superior predictive performance. In the internal validation set, it achieved an accuracy of 0.90, sensitivity of 0.88, specificity of 0.92, and AUC of 0.95 (95% CI 0.91–0.99). These metrics were significantly higher than those of the PET/CT imaging model (accuracy 0.83, sensitivity 0.83, specificity 0.82, AUC 0.85) and clinical model (accuracy 0.65, sensitivity 0.70, specificity 0.59, AUC 0.78). In the external validation set, the model demonstrated an accuracy of 0.81, sensitivity of 0.81, specificity of 0.81, and AUC of 0.85 (95% CI 0.77–0.94), outperforming the PET/CT imaging model (accuracy 0.76, sensitivity 0.75, specificity 0.77, AUC 0.80) and clinical model (accuracy 0.68, sensitivity 0.67, specificity 0.68, AUC 0.76). The nomogram showed excellent calibration, with a C index of 0.98 in the test set, 0.95 in the internal validation set, and 0.91 in the external validation set.

Conclusion: The PET/CT radiomics fusion model significantly improves PI prediction accuracy in NSCLC.

Critical relevance statement: Pleural invasion is a critical prognostic factor in lung cancer and a challenge for preoperative CT evaluation. PET/CT radiomics fusion model has the highest predictive value in predicting PI of lung cancer.

1. Introduction

Lung cancer is one of the most prevalent malignant tumors globally and is associated with a high mortality rate, with NSCLC comprising approximately 80 % of all cases[1]. Surgical resection remains the preferred treatment for patients with early-stage NSCLC. However, the

recurrence rate following surgical resection remains substantial. PI in NSCLC is an independent predictor of poor prognosis and is directly related to the choice of surgical approach[2–4]. For lung cancer nodules smaller than 3 cm with PI, lobectomy is typically recommended[5]. In contrast, for nodules without PI, limited segmentectomy or wedge resection can be employed to maximize preservation of lung function

Abbreviations: AUC, Area under the curve; CTR, Component-to-tumor ratio; DCA, Decision curve analysis; GBDT, Gradient Boosting Decision Tree; HRCT, High-resolution breath-hold CT; SUVmax, Maximum standardized uptake value; NSCLC, Non-small cell lung cancer; PI, Pleural invasion; ROI, Region of interest; VOI, Volume of interest; SVM, Support Vector Machine.

* Corresponding authors at: Key laboratory of Carcinogenesis and Translational Research (Ministry of Education/Beijing), Department of Nuclear Medicine, Peking University Cancer Hospital & Institute, No. 52 Fucheng Rd., Beijing 100142, China.

E-mail addresses: mengxiangxi@pku.edu.cn (X. Meng), rainbow6283@sina.com (N. Li).

¹ Contributed equally to this work.

<https://doi.org/10.1016/j.ejrad.2025.112199>

Received 30 March 2025; Received in revised form 12 May 2025; Accepted 23 May 2025

Available online 24 May 2025

0720-048X/© 2025 Published by Elsevier B.V.

without compromising patient prognosis or survival[6].

Currently, CT-based imaging is the primary method for preoperative evaluation of lung cancer. The assessment of PI largely depends on CT morphological features, such as the pleural tail sign, the size of the solid component of the tumor, and the contact distance between the tumor and the pleura [3,7–10]. However, the interpretation of these features is often subjective and relies heavily on the experience of the radiologist. PET/CT imaging, which incorporates metabolic information, offers distinct advantages over CT morphology alone in evaluating PI in lung cancer. The metabolic parameter maximum standardized uptake value (SUVmax) has been identified as an independent predictor of PI in lung cancer. Studies have demonstrated that SUVmax is positively correlated with the incidence of PI[11], and NSCLC patients with SUVmax ≤ 1.0 are unlikely to have PI[12]. Our previous research has also shown that integrating SUVmax into a PET/CT model significantly improves predictive performance compared to a CT-only model, with the AUC for predicting PI increasing from 0.762 to 0.829[13].

Radiomics leverages deep mining of image data and quantitative analysis of parameters reflecting voxel intensity variations and tumor heterogeneity, uncovering information imperceptible to the human eye. CT radiomics has been applied to PI in lung cancer, with notable studies including Zha et al., who developed a nomogram combining clinical and radiomics features for high accuracy and specificity in PI prediction[14]. Wei et al. explored CT radiomics features for PI in peripheral NSCLC ≤ 3.0 cm, finding that a combined imaging model integrating CT and texture features achieved the highest predictive value for PI, with an AUC of 0.894[15]. Our prior research confirmed that incorporating metabolic features into PET/CT enhances predictive performance for PI compared to CT alone. Building on these findings, integrating CT and PET radiomics features into a PET/CT model is expected to further improve PI prediction. Recent studies have established PET/CT-based radiomics models, including SUVmax, histological grade, nodule-to-pleura distance, and radiomics features, demonstrating potential for non-invasive, personalized PI prediction[16]. However, no multicenter studies have yet reported the use of PET/CT high-dimensional radiomics and PET- radiomics features for predicting NSCLC PI. Our study aims to develop and validate a comprehensive imaging model integrating clinical, morphological, metabolic, and radiomic features for preoperative PI estimation. This PET/CT nomogram can also distinguish high-risk and non-high-risk PI patients non-invasively, aiding clinicians in individualized treatment decisions and prognosis prediction.

2. Materials and methods

2.1. Patient enrollment

This retrospective study was approved by the Institutional Review Committee of Peking University Cancer Hospital, and all methods were conducted in accordance with the approved guidelines, and the requirement for informed consent of patients was waived. We systematically reviewed the records of 1082 lung cancer patients who underwent chest PET/CT scans between January 2018 and December 2022 at Centre A. **The inclusion criteria were as follows:** (1) All patients underwent surgical resection of the lesions, and the presence of PI was confirmed by pathological examination; (2) NSCLC was confirmed pathologically; (3) All patients underwent PET/CT examination within 2 weeks before surgery; (4) Clinical data were available and complete; A total of 371 patients with lung cancer met all inclusion criteria, while 711 patients were excluded for various reasons. The 371 included patients were randomly divided into training (260 patients) and test (111 patients) sets at a 7:3 ratio. Additionally, NSCLC patients collected from August 2021 to August 2024 at Peking University Third Hospital (Centre B) with the same exclusion criteria were included as external test cases, and a total of 99 patients were included. The flow chart of patient enrolment is shown in Fig. 1.

2.2. PET/CT image acquisition

For internal validation patients, ^{18}F -FDG PET/CT was acquired using a Biograph mCT Flow 64 PET/CT scanner (Siemens Healthineers, Erlangen, Germany). All patients fasted for more than 6 h before the examination, with a target blood glucose level of less than 11.1 mmol/L. ^{18}F -FDG was produced in-house (^{18}F was produced by the HM-20 medical cyclotron (Sumitomo Corporation, Japan) with a radiochemical purity greater than 95 %) and injected intravenously (3.0–3.7 MBq/kg). PET/CT images were acquired approximately 60 ± 10 min later. The acquisition range was from the head to the lower thigh. Low-dose nonenhanced CT scanning (120 kV, 146 mAs, slice thickness: 3–5 mm) was used for attenuation correction and anatomical localization, with a matrix of 512×512 . PET scanning was performed in continuous bed motion mode (1.5 min/bed) with a matrix of 200×200 . The ordered subset expectation maximization algorithm was used for PET image reconstruction. High-resolution breath-hold CT(HRCT) of the chest was acquired simultaneously (slice thickness 1 mm, tube voltage peak 120 kVp, tube current 250 mA, rotation time 0.5 s, beam spacing 0.94, matrix 512×512). **For patients in an external test cohort,** the Siemens 52 ring biograph 64 PET/CT was used. ^{18}F -FDG was provided

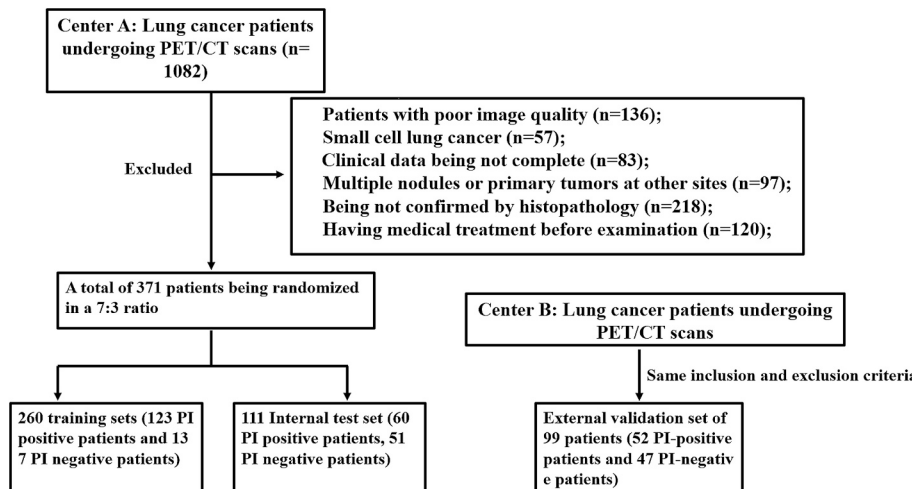


Fig. 1. Flowchart of patient enrollment.

by the Institute of Isotope Research in China Academic of Atomic Energy with radiochemical pure > 90 %. After fasting for more than 6 h, each patient was administered 5.55 MBq/kg ^{18}F -FDG intravenously and imaged with routine PET/CT after 60 min. The CT scans were ranged from the skull base to the upper femur, with matrix of 512×512 . Then, PET images were collected with matrix of 168×168 by 5 ~ 7 beds (2–2.5 min per bed). After that, maintaining the patient position, a deep inspiratory HRCT scan was performed using $64 \times 1.25\text{-mm}$ detectors, with a pitch of 0.53 and 1.25-mm collimation (120 kVp and 100 mAs).

2.3. Image analysis

Two experienced nuclear medicine physicians, with 10 and 16 years of clinical experience, respectively, evaluated PET/CT imaging features in the lung window (window position –700 HU; window width 1500 HU) and mediastinal window (window position 40 HU; window width 400 HU). Discrepancies were resolved through discussion. The CT image features assessed included: (1) tumor density (solid, partially solid, or pure ground-glass nodules); (2) the maximum long diameter of the tumor in the lung window; (3) the maximum long diameter of the solid part of the tumor in the mediastinal window; (4) tumor edge characteristics (lobulation, spiculation); (5) the distance between the tumor and the pleura (minimum distance recorded as negative, contact distance as positive); and (6) the relationship between the tumor and pleura, categorized into five types: Type I (no connection with pleura), Type II (linear shadows to pleura without reaction), Type III (linear shadows with pleural reaction), Type IV (trumpet-shaped pleural depression), and Type V (direct attachment to pleura with traction or pushing). The component-to-tumor ratio (CTR) was defined as the ratio of the solid portion length to the total tumor length. Partial solid nodules were defined as $0 < \text{CTR} < 1.0$, pure solid nodules as $\text{CTR} = 1.0$, and pure ground-glass nodules as $\text{CTR} = 0$. Although previous studies have debated the association between pure ground-glass nodules and pleural invasion, a recent study found that pleural invasion in pure ground-glass nodules should not be overlooked, with an incidence of 17.4 % (12/69) [17]. To ensure comprehensiveness, our study included pure ground-glass nodules. All image data were processed on a Siemens workstation (Syngo.via VB20, MM Oncology). The lesion boundary was manually outlined to obtain the volume of interest (VOI), and the SUVmax was automatically measured. Detailed image feature analysis is provided in the [Supplementary Material 1](#).

2.4. Pathological evaluation

The pathological diagnosis process is independently reviewed by two pathology experts. When opinions are inconsistent, another pathology expert (with more than 10 years of experience) conducts the review. The pathologists evaluated the pathological pattern of the lesion tissue and the T and N stages of the tumor according to the ninth edition of the TNM staging system [18], without knowledge of the imaging results. All surgically resected specimens were stained with hematoxylin and eosin and examined for the presence of PI.

2.5. Construction of prediction model based on radiomics features

Feature extraction: The region of interest (ROI) along tumor margins on CT and PET images was delineated using ITK-SNAP (version 3.8.0). To minimize inter-observer variability, the ROI was manually segmented by two nuclear medicine physicians with over 5 and 10 years of clinical diagnostic experience, respectively. During the segmentation process, neither physician was aware of the patients' final clinical outcomes. The Pyradiomics package in Python (version 3.7.11) was employed to extract radiomic features from the segmented CT and PET image ROIs. Pyradiomics is an open-source Python package designed for extracting radiomic features from medical images. A total of 200 radiomic features were extracted from the CT and PET images. Detailed

descriptions of the extracted radiomic features have been provided in [Supplementary Material 2](#). In the preprocessing step, the ROIs of the CT and PET images were resampled according to their respective resolutions and subsequently standardized using z-score normalization. The detailed preprocessing procedures are provided in the [Supplementary Material 3](#).

Feature screening and model building: Features with an intra-group correlation coefficient (ICC) of less than 0.8 were excluded. Feature screening was performed using six methods: LASSO regression, Chi-square test (CHI2), ordinary least squares (OLS) regression, forward stepwise selection, LightGBM, and XGBoost. This process yielded six distinct groups of features. Each group included 11 clinical indicators, features selected based on clinical and PET/CT imaging criteria, and features selected based on clinical, PET/CT imaging, and PET/CT radiomics criteria. These groups were then used to construct three types of models: clinical model, PET/CT imaging fusion model, and PET/CT radiomics fusion model. For each group of features, 12 machine learning algorithms were employed to construct the clinical model, PET/CT imaging fusion model, and PET/CT radiomics fusion model. These algorithms included Random Forest, Support Vector Machine (SVM), Adaptive Boosting (Adaboost), K-Nearest Neighbors (KNN), Gaussian Naive Bayes (GaussianNB), Bernoulli Naive Bayes (BernoulliNB), Decision Tree, Gradient Boosting Decision Tree (GBDT), Multi-layer Perceptron (MLP), LightGBM, XGBoost, and Logistic Regression. A simplified workflow diagram is illustrated in [Fig. S.1](#). The Rad_score for each patient was calculated as a weighted linear combination of the imaging features selected, using the logistic regression coefficients of these features.

Model performance evaluation: Univariate logistic regression was initially employed to analyze the differences between the PI-negative and PI-positive groups within both the training and validation sets, thereby estimating the relative risk associated with each independent factor. Subsequently, the accuracy of different models was assessed in the test set, while accuracy, specificity, and sensitivity were evaluated in the validation set. The optimal model was selected based on the highest accuracy achieved in the validation set. The discriminatory performance of the clinical model, PET/CT imaging fusion model, and PET/CT radiomics fusion model for PI was further evaluated using the AUC derived from both the training and validation sets.

Nomogram development and evaluation: The radiomics nomogram was developed by integrating non-radiomics features used to construct the optimal model with the Rad_score derived from radiomics features. Through rigorous analysis of the relationship between Rad-score and pathologically confirmed pleural invasion probability in the training set, key cutoff points were determined using the Youden index maximization principle, while incorporating clinical risk stratification needs to establish diagnostic buffer zones. The nomogram's performance in differentiating PI in lung cancer patients was assessed using calibration curves from both the training and validation sets. To evaluate the clinical utility of the nomogram, decision curve analysis (DCA) was employed to calculate the net benefit within the threshold probability range and to determine whether the model could provide clinical benefits to patients. The overall research process is illustrated in [Fig. 2](#). Our entire research process was self-checked through clear checklist ([Table S.1; Supplementary Material 4](#)).

2.6. Statistical analysis

Statistical analyses were conducted using Python (version 3.7.11) and R (version 4.2.2). Continuous variables were assessed using independent t-tests or Mann-Whitney U tests, while categorical variables were evaluated using chi-square tests or Fisher's exact tests. Machine learning models were constructed and ROC curves were generated using the Python package "sklearn." Nomograms and calibration curves were created using the "rms" package in R, and decision curves were drawn using the "rmda" package in R. A p-value of less than 0.05 was

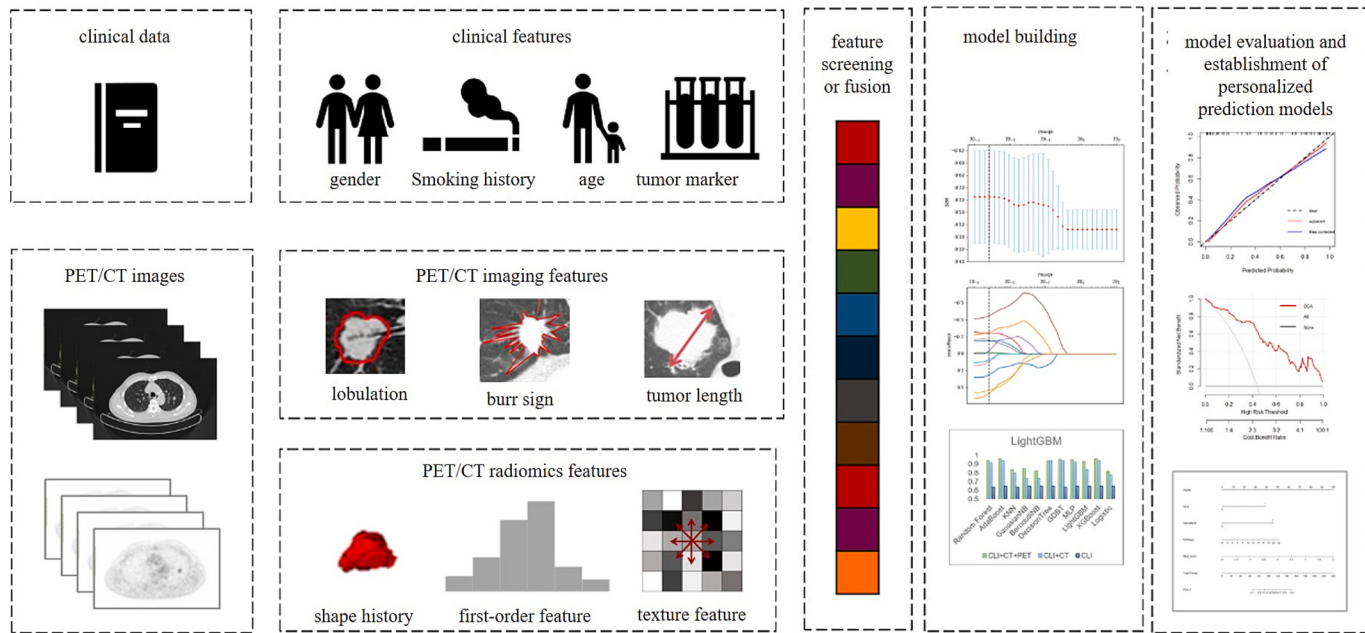


Fig. 2. Overall research process of PET/CT radiomics.

Table 1
Clinical features and PET/CT imaging characteristics.

Characteristic	Training set(n = 260)		Internal validation set(n = 111)		External validation set(n = 99)	
	Negative (n = 137)	Positive (n = 123)	Negative (n = 51)	Positive (n = 60)	Negative (n = 47)	Positive (n = 52)
Clinical features						
Gender						
Male	51(37.2 %)	59(48.0 %)	20(39.2 %)	23(38.3 %)	12(25.5 %)	23(44.2 %)
Female	86(62.8 %)	64(52.0 %)	31(60.8 %)	37(61.7 %)	35(74.5 %)	29(55.8 %)
Age						
Median (IQR) (y)	60 (52,66)	61(54,66)	60(56,68)	60(56,65)	65.5(60.0,72.0)	65.0(56.5,69.5)
Smoke						
No	91(66.4 %)	71(57.7 %)	35(68.6 %)	41(68.3 %)	37(78.7 %)	34(65.4 %)
Yes	46(33.6 %)	52(42.3 %)	16(31.4 %)	19(31.7 %)	10(21.3 %)	18(34.6 %)
CEA						
≤5.0 ng/ml	114(83.2 %)	102(82.9 %)	45(88.2 %)	41(68.3 %)	40(85.1 %)	38(73.1 %)
>5.0 ng/ml	23(16.8 %)	21(17.1 %)	6(11.8 %)	19(31.7 %)	7(14.9 %)	14(26.9 %)
CYFRA21-1						
≤3.3 ng/ml	126(92.0 %)	98(79.7 %)	45(88.2 %)	37(61.7 %)	38(80.1 %)	38(73.1 %)
>3.3 ng/ml	11(8.0 %)	25(20.3 %)	6(11.8 %)	23(38.3 %)	9(19.1 %)	14(26.9 %)
NSE						
≤15.2 ng/ml	99(72.3 %)	83(67.5 %)	40(78.4 %)	33(55.0 %)	39(83.0 %)	40(76.9 %)
>15.2 ng/ml	38(27.7 %)	40(32.5 %)	11(21.6 %)	27(45.0 %)	8(17.0 %)	12(23.1 %)
Thrombus						
No	131(95.6 %)	117(95.1 %)	49(96.1 %)	59(98.3 %)	42(89.4 %)	38(73.1 %)
Yes	6(4.4 %)	6(4.9 %)	2(3.9 %)	1(1.7 %)	5(10.6 %)	14(26.9 %)
Relationship of nodules to the pleura						
I-II	62(45.3 %)	4(3.3 %)	35(68.6 %)	0(0 %)	24(51.1 %)	0(0 %)
III-V	75(54.7 %)	119(96.7 %)	16(31.4 %)	60(100 %)	23(48.9 %)	52(100 %)
PET/CT imaging features						
Spiculation						
No	57(41.6 %)	19(15.4 %)	25(49.0 %)	4(6.7 %)	18(38.3 %)	13(25.0 %)
Yes	80(58.4 %)	104(84.6 %)	26(51.0 %)	56(93.3 %)	29(61.7 %)	39(75.0 %)
Lobulation						
No	49(35.8 %)	0(0 %)	22(43.1 %)	1(1.7 %)	15(31.9 %)	1(1.9 %)
Yes	88(64.2 %)	123(100.0 %)	29(56.9 %)	59(98.3 %)	32(68.1 %)	51(98.1 %)
Major diameter						
Median (IQR) (cm)	1.6(1.4,2.1)	2.9(2.4,3.7)	1.8(1.4,2.1)	2.9(2.4,3.1)	2.1(1.5,2.6)	2.6(2.0,3.0)
CTR						
Median (IQR)	0.2(0,0.5)	0.8(0.6,0.9)	0.2(0,0.5)	0.7(0.6,0.9)	0.5(0.3,0.7)	0.9(0.8,1.0)
Contact distance from the pleura						
Median (IQR) (cm)	-0.4(-1.0,0.6)	1.1(-0.4,2.3)	-0.9(-1.3,-0.4)	1.1(-0.4,2.1)	-0.7(-1.2,-0.4)	1.2(-0.5,2.1)
SUVmax						
Median (IQR)	1.1(0.8,2.7)	6.1(3.4,8.7)	1.6(1.1,2.3)	5.9(3.4,8.7)	1.6(1.2,2.7)	10.3(6.5,12.8)

considered statistically significant.

3. Result

3.1. Clinical data and PET/CT imaging features

Table 1 presents the clinical characteristics and PET/CT imaging features across the training set, internal validation set, and external validation set, as well as between the PI-negative and PI-positive groups.

3.2. Construction of the optimal performance model and Rad score

The performance of each machine learning model, constructed using the six groups of screened features, was compared in the independent validation set to identify the optimal model. The best-performing model was built using GBDT based on features selected by LightGBM. Specifically, the clinical model was constructed using all 11 clinical indicators, the PET/CT imaging fusion model was developed using 9 clinical indicators and 8 PET/CT imaging features, and the PET/CT radiomics fusion model was created using 4 PET/CT imaging features, 16 CT radiomics features, and 3 PET radiomics features. **Fig. 3** illustrates the importance of the selected features. Among the 16 CT radiomics features, there are 5 first-order features, 3 shape features, 4 Gy-level co-occurrence matrix features, 1 Gy-level dependence matrix feature, 2 Gy-level run length matrix features, and 1 Gy-level run matrix feature. All 3 PET radiomics features are shape features. The initial number of extracted features and the final number of selected features for each model are summarized in **Table S.2**. Detailed information on the performance of different machine learning methods in the PET/CT radiomics fusion model is provided in the **Table S.3; Supplementary Material 5**, the feature-related clustering diagram and heatmap, and the model performance corresponding to different numbers of features is provided in the **Supplementary Material 6**. Based on the above 19 radiomics features, logistic regression analysis was used to calculate the correlation weight coefficient of each feature. The Rad score representation of the final radiomics model is detailed in the **Supplementary Material 7**.

3.3. Model performance evaluation

We compared the performance of the three models in internal and external validation sets. In the internal validation set, the clinical model achieved accuracy, sensitivity, and specificity of 0.65, 0.70, and 0.59,

respectively. The PET/CT imaging fusion model achieved accuracy, sensitivity, and specificity of 0.83, 0.83, and 0.82, respectively. The PET/CT radiomics fusion model achieved accuracy, sensitivity, and specificity of 0.90, 0.88, and 0.92, respectively. In the external validation set, the clinical model achieved accuracy, sensitivity, and specificity of 0.68, 0.67, and 0.68, respectively. The PET/CT imaging fusion model achieved accuracy, sensitivity, and specificity of 0.76, 0.75, and 0.77, respectively. The PET/CT radiomics fusion model achieved accuracy, sensitivity, and specificity of 0.81, 0.81, and 0.81, respectively. Overall, the PET/CT radiomics fusion model consistently outperformed the clinical model and the PET/CT imaging fusion model in terms of accuracy, sensitivity, and specificity (**Tables 2**).

In the internal test set, the radiomics fusion model achieved an AUC of 0.95 (95 % CI: 0.91–0.99), which was significantly higher than that of the clinical model (AUC = 0.78, 95 % CI: 0.69–0.87; p < 0.001) and the PET/CT imaging model (AUC = 0.85, 95 % CI: 0.83–0.88; p = 0.115). In the external test set, the radiomics fusion model yielded an AUC of 0.85 (95 % CI: 0.77–0.94), also significantly outperforming the clinical model (AUC = 0.76, 95 % CI: 0.66–0.85; p = 0.013), while showing a non-significant improvement over the PET/CT imaging model (AUC = 0.80, 95 % CI: 0.71–0.90; p = 0.281). ROC curves of the model were

Table 2
Performance of the three models in the different set.

	Clinical model	PET/CT imaging fusion model	PET/CT radiomics fusion model
Training			
Acc	0.75	0.87	0.93
Sen	0.76	0.89	0.94
Spe	0.74	0.85	0.93
AUC	0.82	0.89	0.98
Internal validation			
Acc	0.65	0.83	0.90
Sen	0.70	0.83	0.88
Spe	0.59	0.82	0.92
AUC	0.78	0.85	0.95
External validation			
Acc	0.68	0.76	0.81
Sen	0.67	0.75	0.81
Spe	0.68	0.77	0.81
AUC	0.76	0.80	0.85

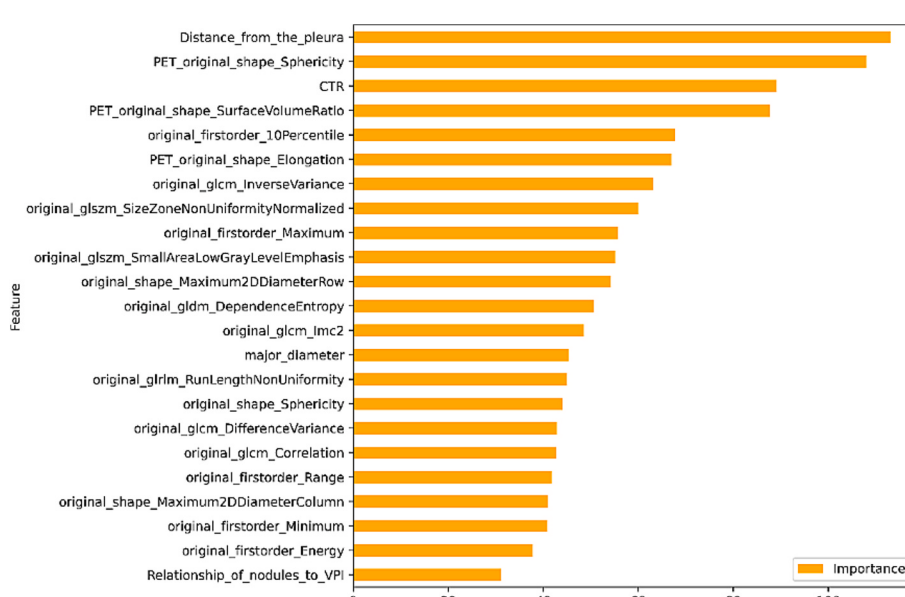


Fig. 3. Importance of selected features (arranged from top to bottom).

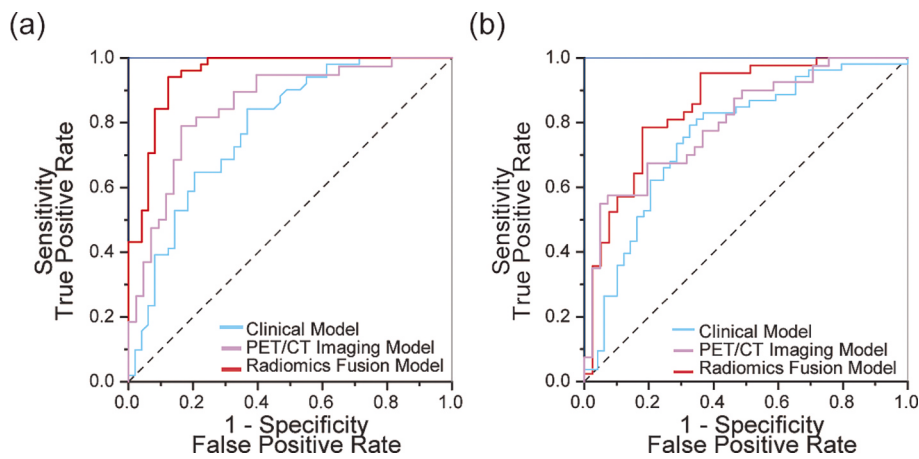


Fig. 4. ROC curves of the model (a internal validation set; b External validation set).

shown in Fig. 4.

3.4. Nomogram construction and evaluation

The four imaging signs (distance between nodules and pleura, relationship between nodules and pleura, CTR, and long diameter of tumor) and Rad_score in the optimal model were incorporated into the radiomics nomogram (Fig. 5). According to the estimation results of the nomogram, if the score is ≤ 60 points, it can be considered that the lesion has almost no PI. For scores between 60–90 points, the lesion has a lower probability of PI (≤ 0.5), and for scores between 90–116 points, the lesion has a higher probability of PI (0.5–0.9). For scores above 120 points, it can be determined that the lesion is combined with PI. The calibration curve confirmed that the nomogram model has good performance in predicting PI. The C index of the nomogram in the training set was 0.98, and the C index reached 0.95 and 0.91 in the internal and external validation sets. The calibration curve showed that the nomogram prediction and the actual data of patients in the training set and validation set had a good consistency of 3.5 (a training set; b internal validation set and c external validation set). The decision curve results of the nomogram in the training set and validation set were shown in Fig. 6 (d training set; e internal validation set and f external validation set). The decision curve analysis demonstrated that the nomogram exhibits a substantial net benefit in differentiating between negative and positive pleural invasion.

4. Discussion

Pleural invasion is an important factor that affects the treatment

decisions and prognosis of lung cancer patients, and it is also a challenge in preoperative CT imaging assessment. As a standard imaging modality for lung cancer, PET/CT integrates anatomical and metabolic information. The potential added value of PET/CT in the preoperative detection of PI is a central focus of this study. In this study, the LightGBM model was used to screen PET/CT imaging features and radiomics features, and the optimal model of GBDT was built to predict PI. The study confirmed that the PET/CT radiomics fusion model has the highest predictive value for predicting PI, and is superior to the PET/CT imaging feature fusion model in both internal and external validation sets. The calibration curve confirmed that the nomogram combining PET/CT imaging features and Rad_score has good performance in predicting PI, and can divide NSCLC into two categories: PI positive and PI negative. The decision curve confirmed that the nomogram can benefit patients in clinical practice.

In this study, the extraction of imaging features was guided by previous research [3,7–10,12], focusing on tumor size, solid component size and proportion, tumor margin, tumor-pleura relationship, tumor-pleura distance, and tumor SUVmax. Variations in sample sizes and disease stages across studies have led to differences in the extracted features. Clinical experience has shown that the accuracy of predicting PI in lung cancer using previously reported imaging features is suboptimal. Radiomics technology addresses this limitation by integrating clinical and imaging data to provide a more comprehensive and accurate prediction of PI. Yuan et al. proposed a deep learning model based on support vector machine (SVM) to predict PI status using preoperative CT scans, achieving high AUC values in the validation cohort[19]. However, this model focused solely on imaging radiomics without incorporating clinical parameters or considering the tumor-pleura relationship.

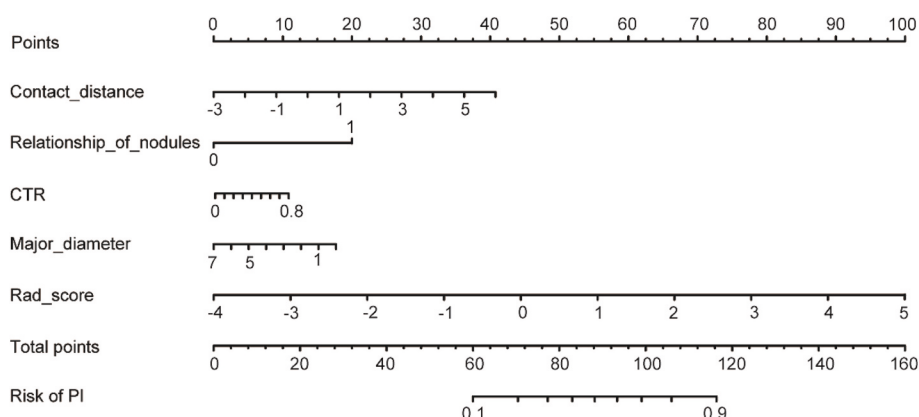


Fig. 5. Radiomics nomogram.

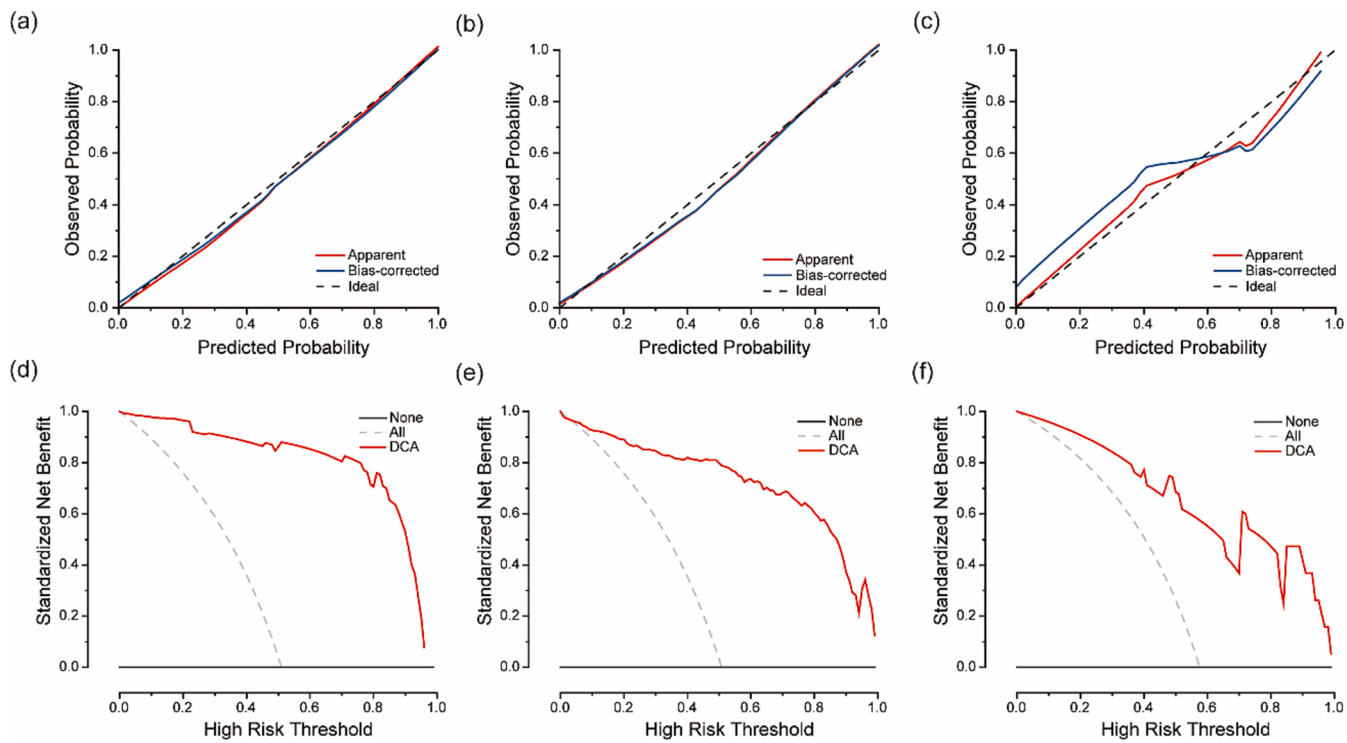


Fig. 6. Calibration curve (a training set; b internal verification set; c external verification set) and decision curve (d training set; e Internal verification set and f external verification set).

Zha et al. developed a combined radiomics model integrating clinical characteristics and CT radiomics features (e.g., coarseness, skewness, total energy) to predict PI, achieving a diagnostic accuracy of 84 % and an AUC of 0.89[14]. They further established a nomogram model with good calibration and predictive performance (Hosmer-Lemeshow test P values of 0.94 and 0.86 in the training and validation cohorts, respectively). However, their study did not include PET radiomics features, limiting the model's comprehensiveness.

As shown in Fig. 3, among all radiomic features, PET_Shape-Sphericity ranked highest in importance, indicating its critical role in model prediction. Biologically, highly aggressive tumors often exhibit irregular and non-spherical morphologies, suggesting their potential for infiltrative growth into surrounding structures. This finding not only confirms the clinical relevance of sphericity as a shape descriptor but also highlights the advantage of PET/CT in simultaneously capturing both metabolic and spatial information. In particular, it underscores the superior performance of PET/CT in identifying complex tumor–pleura interactions compared to CT alone. Through systematic ablation studies, we evaluated the incremental value of PET features. When PET-derived features were excluded, the model's AUC on the external validation set decreased from 0.85 to 0.79. This further supports the incremental value of PET features in enhancing predictive performance.

Our study demonstrates that the combined PET/CT radiomics model built using the GBDT method offers superior predictive value for PI. The fusion model based on Rad_score achieved AUC values of 0.95 and 0.85 in the internal and external validation sets, respectively, outperforming the PET/CT imaging fusion model in the test and training sets (internal test set: AUC = 0.85; external test set: AUC = 0.80). Although some differences in AUC between models did not reach statistical significance, the absolute performance improvements are aligned with clinical needs and still hold practical value. Rad_score captures effective biological information and reflects tumor heterogeneity[20]. It is highly correlated with tumor biological characteristics and invasiveness, and can predict biological marker expression[21], treatment response[22], and survival prognosis[23]. These findings confirm the feasibility of PET/CT

radiomics features in distinguishing high-risk and non-high-risk PI patients. Compared to Rad_score, which focuses on tumor internals, PET/CT imaging features (e.g., lung window diameter, solid component size in the mediastinal window, spiculation sign, lobulation sign, nodule-pleura distance, and nodule-pleura relationship) describe tumor circumference, external morphology, and peritumoral characteristics. The PET/CT Rad_score and imaging feature models are complementary; only by integrating both external and internal tumor characteristics can the nature of the tumor be fully reflected, maximizing the distinction between high-risk and non-high-risk PI patients. Our combined PET/CT radiomics model outperforms previously reported CT radiomics models [24–27], highlighting the added predictive value of PET radiomics for PI. The nomogram integrating PET/CT imaging features and Rad_score has been validated to perform exceptionally well in predicting PI, offering tangible benefits in clinical practice.

There are some limitations in this study. First, the study excluded patients who had received treatment prior to ¹⁸F-FDG PET/CT imaging or who did not undergo pathological confirmation after PET/CT imaging. This may have limited the clinical applicability of the study. Secondly, the generated radiomics model and nomogram need to be prospectively validated to prepare for later clinical application. This validation is particularly critical to address potential overfitting risks arising from high-dimensional data and small sample sizes during model development. Finally, more external validation and larger data sets are needed to validate and improve our results. Specifically, reproducibility metrics across different scanners or institutions should be prioritized to ensure robustness in diverse clinical settings.

5. Conclusions

In conclusion, the PET/CT radiomics fusion model has a high predictive value for predicting PI in NSCLC, and is superior to the PET/CT image feature fusion model in the internal and external validation sets, and can identify high-risk patients with PI. We have developed and validated the ¹⁸F-FDG PET/CT radiomics nomogram for distinguishing

high-risk and non-high-risk groups of patients with PI in lung cancer, which is helpful for personalized and precise treatment for lung cancer patients.

Declarations:

Ethics approval and consent to participate.

Our institutional review board approved this retrospective study, and so, the requirement for informed consent was waived.

Consent for publication

All authors agreed to submit and further publicize this paper.

Availability of data and material.

The datasets used or analyzed during the current study are available from the corresponding author upon reasonable request.

Funding.

The current research was financially supported by Key Clinical Project of Peking University Third Hospital (BYSYZD2024043).

CRediT authorship contribution statement

Annan Zhang: Writing – review & editing, Writing – original draft, Validation, Software, Methodology, Conceptualization. **Meixin Zhao:** Software, Methodology, Conceptualization. **Xiangxing Kong:** Writing – original draft, Validation, Software. **Weifang Zhang:** Visualization, Investigation. **Xiaoyan Hou:** Validation, Software. **Zhi Yang:** Supervision. **Xiangxi Meng:** Writing – review & editing, Visualization, Validation, Supervision, Investigation. **Nan Li:** Writing – review & editing, Supervision.

Declaration of competing interest

The authors declare that they have no known competing financial interests or personal relationships that could have appeared to influence the work reported in this paper.

Appendix A. Supplementary data

Supplementary data to this article can be found online at <https://doi.org/10.1016/j.ejrad.2025.112199>.

References

- [1] H. Sung, J. Ferlay, R.L. Siegel, M. Laversanne, I. Soerjomataram, A. Jemal, et al., Global Cancer Statistics 2020: GLOBOCAN Estimates of Incidence and Mortality Worldwide for 36 Cancers in 185 Countries, *Ca-a Cancer Journal for Clinicians*. 71 (3) (2021) 209–249, <https://doi.org/10.3322/caac.21660>.
- [2] J. Yoshida, K. Nagai, H. Asamura, T. Goya, Y. Koshiishi, Y. Sohara, et al., Visceral pleura invasion impact on non-small cell lung cancer patient survival: its implications for the forthcoming TNM staging based on a large-scale nation-wide database, *J. Thorac. Oncol.* 4 (8) (2009) 959–963, <https://doi.org/10.1097/JTO.0b013e3181a85d5e>.
- [3] Sun Q, Li P, Zhang J, Rowena Y , Zhu Y, David F, et al, CT Predictors of Visceral Pleural Invasion in Patients with Non-Small Cell Lung Cancers 30 mm or Smaller. *Radiology* 310(1) (2024) e231611, <http://doi: 10.1148/radiol.231611>.
- [4] Y. Wang, F. Qian, M. Hu, Y. Chen, Z. Yang, B. Han, Clinical significance of visceral pleural and lymphovascular invasion in surgically resected adenosquamous lung cancer, *Eur. J. Cardiothorac. Surg.* 59 (3) (2021) 617–623, <https://doi.org/10.1093/ejcts/ezaa353>.
- [5] Huang W, Deng H, Lin M, Xu K, Zhang Y, Yuan C, et al Treatment Modality for Stage IB Peripheral Non-Small Cell Lung Cancer With Visceral Pleural Invasion and </=3 cm in Size. *Frontiers in Oncology* 12 (2022) 830470, <http://doi: 10.3389/fonc.2022.830470>.
- [6] Tsutani Y, Nakayama H, Ito H, Handa Y, Mimae T, Miyata Y, et al Long-Term Outcomes After Sublobar Resection Versus Lobectomy in Patients With Clinical Stage IA Lung Adenocarcinoma Meeting the Node-Negative Criteria Defined by High-Resolution Computed Tomography and [(18)F]-Fluoro-2-Deoxy-d-Glucose Positron Emission Tomography. *Clinical Lung Cancer* 22(3) (2021) e431-e437, <http://doi: 10.1016/j.cllc.2020.06.013>.
- [7] Hsu J, Han I, Tsai T, Lin S, Jaw T, Liu G, et al Pleural Tags on CT Scans to Predict Visceral Pleural Invasion of Non-Small Cell Lung Cancer That Does Not Abut the Pleura. *Radiology* 279(2) (2016) 590-596, <http://doi: 10.1148/radiol.201515120>.
- [8] K. Imai, Y. Minamiya, K. Ishiyama, M. Hashimoto, H. Saito, S. Motoyama, et al., Use of CT to evaluate pleural invasion in non-small cell lung cancer: measurement of the ratio of the interface between tumor and neighboring structures to maximum tumor diameter, *Radiology* 267 (2) (2013) 619–626, <https://doi.org/10.1148/radiol.12120864>.
- [9] Onoda H, Higashi M, Murakami T, Tao H, Yokoyama S, Kunihiro Y, et al, Correlation between pleural tags on CT and visceral pleural invasion of peripheral lung cancer that does not appear touching the pleural surface. *European Radiology* 31(12) (2021) 9022-9029, <http://doi: 10.1007/s00330-021-07869-y>.
- [10] Chen Z, Jiang S, Li Z, Rao L, Zhang X, Clinical Value of (18)F-FDG PET/CT in Prediction of Visceral Pleural Invasion of Subsolid Nodule Stage I Lung Adenocarcinoma. *Academic Radiology* 27 (12) (2020)1691-1699, <http://doi: 10.1016/j.acra.2020.01.019>.
- [11] R. Maeda, N. Isowa, H. Onuma, H. Miura, T. Harada, H. Touge, et al., The maximum standardized 18F-fluorodeoxyglucose uptake on positron emission tomography predicts lymph node metastasis and invasiveness in clinical stage IA non-small cell lung cancer, *Interact. Cardiovasc. Thorac. Surg.* 9 (1) (2009) 79–82, <https://doi.org/10.1510/icvts.2008.201251>.
- [12] T. Tanaka, T. Shinya, S. Sato, T. Mitsuhashi, K. Ichimura, J. Soh, et al., Predicting pleural invasion using HRCT and 18F-FDG PET/CT in lung adenocarcinoma with pleural contact, *Ann. Nucl. Med.* 29 (9) (2015) 757–765, <https://doi.org/10.1007/s12149-015-0999-x>.
- [13] A. Zhang, X. Meng, Y. Yao, X. Zhou, S. Yan, W. Fei, et al., Predictive Value of (18)F-FDG PET/MRI for Pleural Invasion in Solid and Subsolid Lung Adenocarcinomas Smaller Than 3 cm, *J. Magn. Reson. Imaging* 57 (5) (2023) 1367–1375, <https://doi.org/10.1002/jmri.28422>.
- [14] X. Zha, Y. Liu, X. Ping, J. Bao, Q. Wu, S. Hu, et al., A Nomogram Combined Radiomics and Clinical features as imaging biomarkers for prediction of visceral pleural invasion in lung adenocarcinoma, *Front. Oncol.* 12 (2022), <https://doi.org/10.3389/fonc.2022.876264>.
- [15] Wei S, Zhang J, Shi B, Gao F, Zhang Z, Qian L, The value of CT radiomics features to predict visceral pleural invasion in </=3 cm peripheral type early non-small cell lung cancer. *Journal of X-Ray Science and Technology* 30 (6) (2022) 1115-1126, <http://doi: 10.3233/XST-221220>.
- [16] Cui N, Li J, Jiang Z, Long Z, Liu W, Yao H, et al Development and validation of (18)F-FDG PET/CT radiomics-based nomogram to predict visceral pleural invasion in solid lung adenocarcinoma. *Annals of Nuclear Medicine* 37 (11) (2023)605-617, <http://doi: 10.1007/s12149-023-01861-w>.
- [17] Zhao L, Xie H, Zhang L, Zha J, Zhou F, Jiang G, et al, Visceral pleural invasion in lung adenocarcinoma </=3 cm with ground-glass opacity: a clinical, pathological and radiological study. *Journal of Thoracic Disease* 8(7) (2016) 1788-1797, <http://doi: 10.21037/jtd.2016.05.90>.
- [18] Detterbeck FC, Woodard GA, Bader AS, Dacic S, Grant MJ, Park HS, et al, 2024 The Proposed Ninth Edition TNM Classification of Lung Cancer. *Chest* 166(4) 882-895 [10.1016/j.chest.2024.05.026](http://doi: 10.1016/j.chest.2024.05.026).
- [19] M. Yuan, J. Liu, T. Zhang, Y. Zhang, H. Li, T. Yu, Prognostic Impact of the Findings on Thin-Section Computed Tomography in stage I lung adenocarcinoma with visceral pleural invasion, *Sci. Rep.* 8 (1) (2018) 4743, <https://doi.org/10.1038/s41598-018-22853-1>.
- [20] E.L. Solari, A. Gafita, S. Schachoff, B. Bogdanović, A.V. Asiales, T. Amiel, et al., The added value of PSMA PET/MR radiomics for prostate cancer staging, *Eur. J. Nucl. Med. Mol. Imaging* 49 (2) (2022) 527–538, <https://doi.org/10.1007/s00259-021-05430-z>.
- [21] Li X, Xu C, Yu Y, Guo Y, Sun H, Prediction of lymphovascular space invasion using a combination of tenascin-C, cox-2, and PET/CT radiomics in patients with early-stage cervical squamous cell carcinoma. *Bmc Cancer* (1) 2021 866 10.1186/s12885-021-08596-9.
- [22] Liu Z, Wang S, Dong D, Wei J, Fang C, Zhou X, et al The Applications of Radiomics in Precision Diagnosis and Treatment of Oncology: Opportunities and Challenges. *Theranostics* 9(5) (2019) 1303-1322 10.7150/thno.30309.
- [23] X. Wang, T. Xie, J. Luo, Z. Zhou, X. Yu, Guo X Radiomics predicts the prognosis of patients with locally advanced breast cancer by reflecting the heterogeneity of tumor cells and the tumor microenvironment, *Breast Cancer Res.* 24 (1) (2022) 20, <https://doi.org/10.1186/s13058-022-01516-0>.
- [24] X. Cai, P. Wang, H. Zhou, H. Guo, X. Yang, Z. Dai, et al., CT-based radiomics nomogram for predicting visceral pleural invasion in peripheral T1-sized solid lung adenocarcinoma, *Am. J. Cancer Res.* 13 (12) (2023) 5901–5913.
- [25] F. Wang, X. Pan, T. Zhang, Y. Zhong, C. Wang, H. Li, et al., Predicting visceral pleural invasion in lung adenocarcinoma presenting as part-solid density utilizing a nomogram model combined with radiomics and clinical features, *Thoracic Cancer* 15 (1) (2024) 23–34, <https://doi.org/10.1111/1759-7714.15151>.
- [26] Zuo Y, Gao D, Cui J, Gao Z, Feng P, Geng Z, et al, Peritumoral and intratumoral radiomics for predicting visceral pleural invasion in lung adenocarcinoma based on preoperative computed tomography (CT). *Clinical Radiology* 80(2025) 106729, <http://doi: 10.1016/j.crad.2024.10.010>.
- [27] Y. Wang, D. Lyu, S. Hu, Y. Ma, S. Duan, Y. Geng, et al., Nomogram using intratumoral and peritumoral radiomics for the preoperative prediction of visceral pleural invasion in clinical stage IA lung adenocarcinoma, *J. Cardiothorac. Surg.* 19 (1) (2024) 307, <https://doi.org/10.1186/s13019-024-02807-7>.